THE ASTROPHYSICAL JOURNAL, 318:595–611, 1987 July 15

THE CONTINUUM OF TYPE 1 SEYFERT GALAXIES. II. SEPARATING THERMAL AND NONTHERMAL COMPONENTS[1]

N. P. CARLETON, MARTIN ELVIS, G. FABBIANO, AND S. P. WILLNER
Harvard-Smithsonian Center for Astrophysics

A. LAWRENCE
Queen Mary College, London

AND

MARTIN WARD
Institute of Astronomy, Cambridge, England; and Astronomy Department, University of Washington
Received 1986 October 8; accepted 1986 December 24

ABSTRACT

We attempt to distinguish between thermal and nonthermal contributions to the 1 to 100 μm continuum in a sample of active galactic nuclei. The sample is dominated by the members of a hard X-ray selected complete sample; all galaxies in the sample have been measured in hard X-rays, and most turn out to be Seyfert 1 galaxies. We postulate that the nonthermal continua of all the objects are intrinsically similar, with the apparent "steep spectrum" objects showing a combination of reddening at shorter wavelengths and thermal emission by dust at longer wavelengths. Correlations between infrared, hard X-ray, and emission-line luminosities give considerable evidence for this hypothesis; for example, a simply defined upper limit for the nonthermal component in the infrared is better correlated with the hard X-ray luminosity than is the flux density at any individual wavelength. Moreover, extrapolation of the observed steep spectra suggests a deficiency of ionizing photons; dereddening would remove this deficiency. We conclude that, in general, the objects with the flattest energy distributions are mainly nonthermal but may have thermal contributions at wavelengths that differ in different objects, while the objects with steep spectra are mainly thermal except at wavelengths shorter than ~ 2 μm. The inferred dust distributions can have substantial covering factors and extend over much the same range of distances from the nuclei as the emission-line regions.

Subject headings: galaxies: Seyfert — infrared: spectra — spectrophotometry

I. INTRODUCTION

A preceding paper (Ward *et al.* 1987, hereafter Paper I) examined the optical to far-infrared energy distributions of Seyfert 1 galaxies. Although the observed energy distributions have a confusing variety of forms, Paper I suggested that these could be primarily the result of two simple effects. One effect was well-established and is no surprise: stars and cool dust in the host galaxy contaminate the emission from the nucleus. This contamination is especially important for low-luminosity nuclei. The other effect was suggested but not firmly established: dust near the nucleus may absorb optical and ultraviolet light and reemit it thermally in the infrared.

There has been a continuing debate about whether the infrared continua of Seyfert 1 galaxies are thermal or nonthermal. Stein and Weedman (1976) found evidence of a substantial nonthermal component at 3.5 μm. Edelson and Malkan (1986, hereafter EM) go further, attributing the bulk of the emission at all infrared wavelengths to nonthermal emission. On the other hand, Rieke and Lebofsky (1981) found that NGC 4151 varied much less in the infrared than in the optical and contended that the bulk of the emission beyond 1 μm is thermal emission from dust. MacAlpine (1985) has made a strong case that reddening affects the visible and ultraviolet lines, and thus dust must be present. Rieke (1985) has reviewed much additional evidence and concludes that thermal emission is important for at least some objects.

This paper takes a relatively simple but somewhat novel approach. We introduce an empirical method for decomposing the infrared (1–100 μm) continuum into thermal and nonthermal components. Based on the results, we postulate that all Seyfert 1 nuclei could have the same underlying continuum energy distribution, which is modified by dust absorption and thermal reemission. We then examine additional evidence and find that this interpretation of the infrared continuum is supported by a variety of data. Finally, we address the spatial and temperature distribution of the infrared-emitting dust component in the nucleus and its relation to central source luminosity.

The decomposition into thermal and nonthermal components (§ II) is based on indirect clues from comparison of the infrared emission to that at other wavelengths. For example, there are strong reasons for believing that the X-ray emission comes from a very compact region (see, e.g., Rees, Begelman, and Blandford 1981), while the optical forbidden-line emission is much more extended (Wilson and Heckman 1985). Evidence that the strength of the infrared emission is closely related to either of these would suggest that it comes from the same region. We have therefore collected emission-line data for the Seyfert nuclei, together with hard X-ray luminosities, and we search for the strongest correlations between these quantities and continuum emission at various wavelengths. The result is

[1] Based on data taken at the Infrared Telescope Facility, which is operated by the University of Hawaii under contract with the National Aeronautics and Space Administration, and the Cerro Tololo Inter-American Observatory, National Optical Astronomy Observatories, operated by the Association of Universities for Research in Astronomy, Inc., under contract with the National Science Foundation.

that we can define an infrared continuum level that is highly correlated with the hard X-rays.

Testing the hypothesis that the empirical decomposition really differentiates between thermal and nonthermal components is not easy. If the dust were uniformly and spherically distributed about the source, then the testing of the hypothesis would be straightforward. In reality, we must expect that attenuation in our line of sight may not be representative of the whole, owing either to random patchiness of the dust, or to the existence of some structure like a toroid or thick disk whose orientation varies from object to object, as suggested, for example, by Lawrence and Elvis (1982). It is therefore necessary to look at the properties of a large sample of objects. As our sample is dominated by the members of the complete hard X-ray selected sample of Piccinotti *et al.* (1982), it is biased neither toward nor away from objects containing dust. This makes it singularly valuable for a study of the importance of dust in active galactic nuclei (AGNs). Section III first shows that reddening is important for the visible and ultraviolet continua, as well as the emission lines (MacAlpine 1985). It then shows that infrared emission at a variety of wavelengths correlates with reddening measures, as would be expected for thermal reemission. Finally, we examine the implied distribution of the dust and find it to be plausible.

II. A UNIVERSAL CONTINUUM

Paper I divided our sample into three groups based on the energy distributions. Typical energy distributions are shown in Figure 1, and the data for the entire sample were shown in Figure 1 of Paper I. Of the original sample of 34 galaxies, nine appeared to have strong contamination from the host galaxy, both from cool dust emission at 60–100 μm and from starlight, and these objects were designated class C. Four more galaxies had insufficient data to be classified. The remaining 21 galaxies were separated based on the ratio of 0.36 μm to 1.2 μm flux densities. We assumed that those objects with the greatest relative ultraviolet flux densities are the least reddened and therefore have the least potential for thermal infrared emission; these 12 objects were designated class A. This left nine objects (class B) that we consider as candidates for substantially reddened AGNs.

a) Underlying Nonthermal Component

Our first task is to define a plausible nonthermal component in the infrared. Nonthermal processes are usually considered in terms of power-law spectra. Empirically this seems to be a good approximation at least in sections of the continuum, such as the infrared, covering one or two decades in frequency. Even for objects in which a higher degree polynomial (e.g., a parabola) gives a better fit to the radio through ultraviolet continuum, the curvature is slight in the infrared (Landau *et al.* 1986). We therefore make the assumption that a single power law underlies the whole 1–100 μm region. An upper limit on this component is a straight line through the lowest two points in a plot of log $\nu f(\nu)$ versus log ν, as indicated in Figure 1. An infrared power law should be most easily distinguished for class A objects. Figure 2*a* shows the distribution of power-law slopes [for $f(\nu) \propto \nu^{\alpha}$] for the 12 objects in class A, and the indices are listed individually in Table 1. The average index for the class A objects is $\alpha_{IR} = -1.02 \pm 0.10$. The small dispersion among power-law slopes suggests that a power-law baseline under the infrared region with an index $\alpha \approx -1$ may indeed be a physically meaningful component.

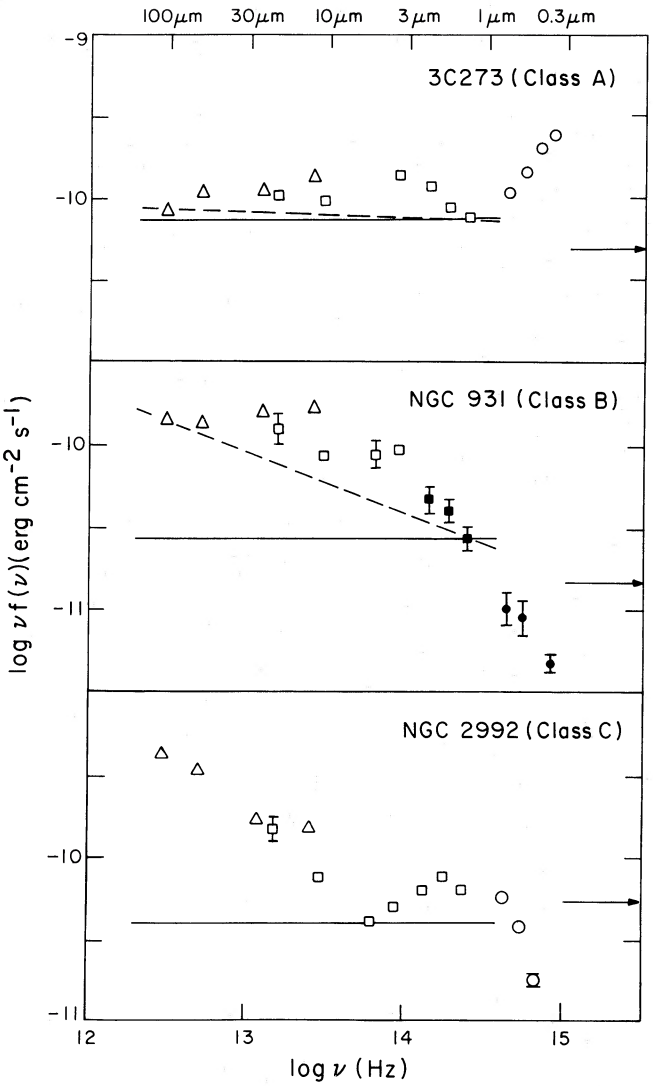

FIG. 1.—The infrared to ultraviolet energy distribution [log $\nu f(\nu)$ vs. log ν] of a typical object in each class defined in Paper I. Triangles are *IRAS* data points, squares are ground-based *JHKLMNQ* infrared data points, and circles are *UBVR* photometry. The arrows on the right margin indicate the level of the 6 keV flux densities. Starlight has been subtracted only from the NGC 931 data; see Paper I for details and references. The dashed lines denote the power-law fit through the two lowest points in the infrared; the slopes of these lines comprise the data shown in Fig. 2*a*. The solid lines denote the "infrared baselines" drawn through the single lowest point; these represent the values of IR_b used in the correlation analysis.

A power law with $\alpha = 1.0$ is very attractive as a general approximation to an underlying nonthermal spectrum, as it represents the simple case of constant power per unit logarithmic bandwidth—a horizontal line on our plots of $\nu f(\nu)$ versus ν. If we assume that such a power law may be present in all our spectra, then we have a way of making a provisional separation of thermal and nonthermal components: find the lowest point in a plot of $\nu f(\nu)$ in the range 1–100 μm and draw a horizontal line through it. We refer to this lowest value of $\nu f(\nu)$ as the "infrared baseline," IR_b. The power represented by the area under the infrared baseline is potentially nonthermal, while the power represented by the area above the line and below the actual data points is potentially thermal. (The power above the infrared baseline may include components of starlight and

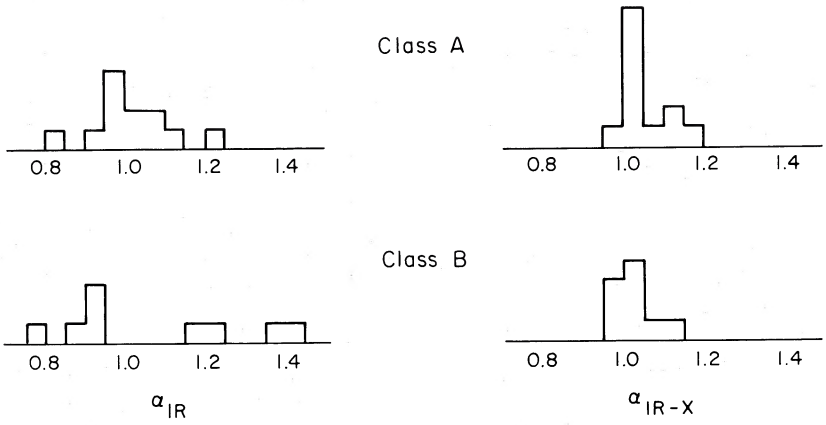

FIG. 2.—(*a–b*) The distribution of power-law indices for class A and class B objects. The left side (*a*) shows the indices α_{IR} derived from the lowest two points in the infrared, and the right side (*b*) shows the indices α_{IR-X} derived by connecting the 1.25 μm flux density of the infrared baseline with the hard X-rays.

TABLE 1

OBSERVED BALMER DECREMENTS AND POWER-LAW PARAMETERS

Object	z	Hα/Hβ[a]	α_{IR}	λ_B[b]	λ_s[c]	L_{above}/L_{below}	log L_{below}[d]	log L_{above}[e]
Class A								
III Zw 2[f]	0.0898	3.6	−1.08	1.6	10.2	0.18	45.47	44.73
F9[f]	0.0461	...	−0.93	10.2	1.2	0.34	45.49	45.02
Akn 120	0.0325	4.2	−0.85	60	1.2	0.48	44.82	44.50
Mkn 79	0.0222	5.9	−1.21	1.2	100	1.19	44.39	44.47
NGC 3783	0.0091	2.9	−0.95	2.2	1.2	1.57	43.84	44.04
NGC 4151	0.0033	3.6	−1.04	1.2	100	1.08	43.53	43.56
3C 273	0.158	3.1	−1.03	1.2	100	0.41	46.61	46.22
NGC 5548	0.0166	5.3	−0.99	100	1.2	0.22	44.42	43.76
Mkn 1383[f]	0.086	...	−1.09	1.2	20	0.14	45.42	44.57
Mkn 841	0.0366	4.8	−1.12	1.2	60	1.04	44.62	44.64
ESO 141−G55	0.0368	3.7	−0.96	100	1.2	0.48	44.91	44.59
Mkn 509	0.0352	2.8	−0.95	100	1.6	0.69	44.99	44.83
Class B								
NGC 526a	0.0189	>18	−0.93	2.2	60	0.86	44.24	44.17
NGC 931	0.0163	6.3	−1.39	1.2	100	2.71	44.14	44.57
3C 120	0.0330	4.9	−0.94	1.2	100	1.17	44.76	44.83
MCG 8-11-11	0.0205	6.5	−1.40	1.2	100	4.06	44.27	44.88
3A 0557−385	0.0344	18	−0.90	1.2	60	1.63	44.82	45.03
MCG −6-30-15	0.0078	5.1	−0.87	100	1.2	1.36	43.54	43.67
IC 4329A	0.0138	13.2	−0.75	100	1.2	2.91	44.23	44.69
NGC 5506	0.0061	6.7(N)	−1.21	1.2	100	1.43	43.87	44.03
ESO 103−G35	0.013	12.6	−1.16	3.5	100	3.51	43.91	44.46
Class C								
NGC 2992	0.0073	11.5(N)	...	4.8	...	2.33	43.61	43.98
NGC 3227	0.0033	5.1	...	4.8	...	2.92	42.97	43.44
NGC 4051	0.0023	4.3	...	1.6	...	0.77	42.65	42.54
NGC 4593	0.0085	3.3	...	10.2	...	0.61	43.87	43.66
NGC 7172	0.009	...	...	10.2	...	2.18	43.80	44.14
NGC 7213	0.0058	6.2	...	20	...	...	43.75	...
NGC 7314	0.0056	19.2(N)	...	4.8	...	3.65	43.00	43.56
NGC 7469	0.0167	5.6	...	1.2	...	3.40	44.72	45.25
NGC 7582	0.0053	...	...	1.2	...	5.41	43.68	44.41

[a] See Table 2 for references.
[b] λ_B = wavelength of minimum value of $vf(v)$, between 1 and 100 μm.
[c] λ_s = second point used with λ_B to define α_{IR}.
[d] $L_{below} = [IR_b] \times \ln(100/1.2)$.
[e] $L_{above} = L_{observed} - L_{below}$.
[f] *IRAS* data missing for these objects; parameters defined on available data.

galactic dust emission in addition to the emission from hot circumnuclear dust or dense gas.) Table 1 lists the wavelength, λ_B, where the baseline is defined for each object and the luminosities above and below the baseline. Figure 1 shows how different this baseline is from any power law that might be suggested by the raw data for typical objects in class B and class C.

b) Infrared and X-ray Continuum Correlations

To examine the significance of the infrared baseline, and to study in general the relation between the luminosities measured at different wavelengths and in emission lines, we have performed a formal analysis of correlations between these quantities. A detailed description of the method and tables of the data and results (Tables 2–4) are presented in the Appendix.

The 6 keV radiation is a particularly useful indicator of nonthermal radiation, because variability observations and arguments concerning energy imply that hard X-rays must certainly originate in the central source. Moreover, their attenuation by gas or dust is less than 1 mag for column densities less than 6×10^{23} atoms cm^{-2} (Zombeck 1982). Figure 3 shows the correlations between luminosities in X-rays and in several lower frequencies, omitting those at which contamination from starlight could be the greatest. For reference, each plot shows a line of unit slope passing through the point representing 3C 273, the most luminous and the most UV-rich object in the sample.

All of the line and continuum luminosities are correlated with high significance (Table 3) but with varying degrees of scatter. This implies that to first order the entire AGN phenomenon simply scales with luminosity. Véron-Cetty, Véron, and Tarenghi (1983) reached a similar conclusion through studying the ultraviolet spectra of AGNs. Shuder (1981) found that the scaling holds over a variety of types of AGN including Seyfert 1's and extending over a range of more than 4 decades in luminosity.

Figure 3 shows that the correlation of [3.5 μm] with [6 keV][2] stands out as the relation with the least scatter (Malkan 1984) and the least dependence on luminosity of the directly observed quantities. Figure 3 also shows the correlation between the infrared baseline IR_b and the hard X-ray luminosity. This correlation is the best of all. The quantitative result of the partial Spearman rank test, listed in Table 4, shows that for the complete sample of A and B objects, IR_b is indeed significantly *better* correlated with [6 keV] than is [3.5 μm] with [6 keV]. This suggests that the correlation of IR_b with [6 keV] is the more fundamental correlation (see discussion in the Appendix). It thus appears that the infrared baseline indeed defines a value for a nonthermal infrared component with a strong, nonluminosity-dependent correlation with the X-ray region.

Further information on the infrared baseline can be obtained by comparing its actual flux density to the hard X-ray flux density. We make the comparison by defining an index α_{IR-X} for the power law that connects the 1 μm end of the infrared baseline to the 6 keV point. The results of this exercise are listed in Table 1 and displayed in Figure 2. The average value for the 12 class A objects is $\alpha_{IR-X} = -1.05 \pm 0.05$ and for the nine class B objects is $\alpha_{IR-X} = -1.03 \pm 0.04$. First, it is interesting that these values are so close to the average value $\alpha_{IR} = -1.02$ that characterizes the class A objects in the infrared. Second, the identity of the α_{IR-X} values for the two classes again implies that our method of selecting IR_b is meaningful, in spite of the wide variation of apparent infrared slopes that might be inferred from the class B spectra (as shown in Fig. 2 and Table 1).

The fact that the 6 keV point is on an extrapolation of the infrared power law for this sample of objects does not necessarily mean that a single power law must extend over the intervening frequencies. In fact, the measured slopes in the X-ray for this sample are $\alpha_X \approx 0.7$ (Petre *et al.* 1984; Mushotzky 1984), and therefore the presence of another component is indicated. On the other hand, a single power law covering the infrared to X-ray region has been suggested for a sample of optically selected quasars (Elvis *et al.* 1986) and for several BL Lac objects (Madejski 1985) and is physically reasonable. Several classes of models exist that can produce such an extended power law (see discussion by Elvis *et al.* 1986), including direct synchrotron emission, unsaturated Comptonization of an infrared synchrotron spectrum, and self-Compton emission of infrared synchrotron producing electrons. A plausible explanation of the hard X-ray emission is that it is a combination of the power law extended from the infrared and a flatter component that dominates at higher energies. This explanation appears satisfactory for 3C 273, where $vf(v)$ goes on rising into the 100 keV region (Bezler *et al.* 1984). We emphasize, however, that our conclusions regarding the infrared emission do not depend on the physical mechanism for the X-ray emission or on the extrapolation of the infrared power law to shorter wavelengths. Rather the key assumption in establishing the physical significance of the infrared baseline is that the X-rays are directly indicative of the central source luminosity.

c) A Common Central-Source Spectrum

The data suggest that all objects have an emission component that can be closely represented as a power law with an index near -1.0. Many objects also show a strong upturn in the blue, suggesting another component interpreted by Malkan and Sargent (1982) as thermal emission from an accretion disk. There is little evidence for how much this component, referred to as the "big bump," may change from object to object relative to the power law. For definiteness in the discussion that follows, we will consider that a truly unreddened spectrum might look like that of 3C 273, a well-observed object that has as much ultraviolet flux as any object in our sample. Figure 4 shows the observations of 3C 273 along with the assumed form for the underlying central source spectrum. The ultraviolet portion of the assumed central source spectrum is based on the data and analysis of Malkan and Sargent (1982) but includes a more conservative reddening correction amounting to $A_V = 0.17$ mag, compared to $A_V = 0.28$ derived by Malkan and Sargent. Considering that most of the adopted reddening is the Galactic value implied by 21 cm observations, we consider it unlikely that the actual ultraviolet flux is less than the amount shown, and even a reduction by the maximum factor of 2 would not significantly change the results of this paper. The presentation of Figure 4 as a linear plot of $vf(v)$ against log v is particularly useful in that an area under the plotted spectrum, between two values of log v, represents the power actually radiated in that frequency band. The linear plot of $vf(v)$ emphasizes how large a contribution the big bump makes to the overall energy budget, even with this conservative

[2] Here and subsequently we shall use, e.g., [20 μm] to stand for the luminosity corresponding to $vf(v)$, where v is the frequency corresponding to 20 μm.

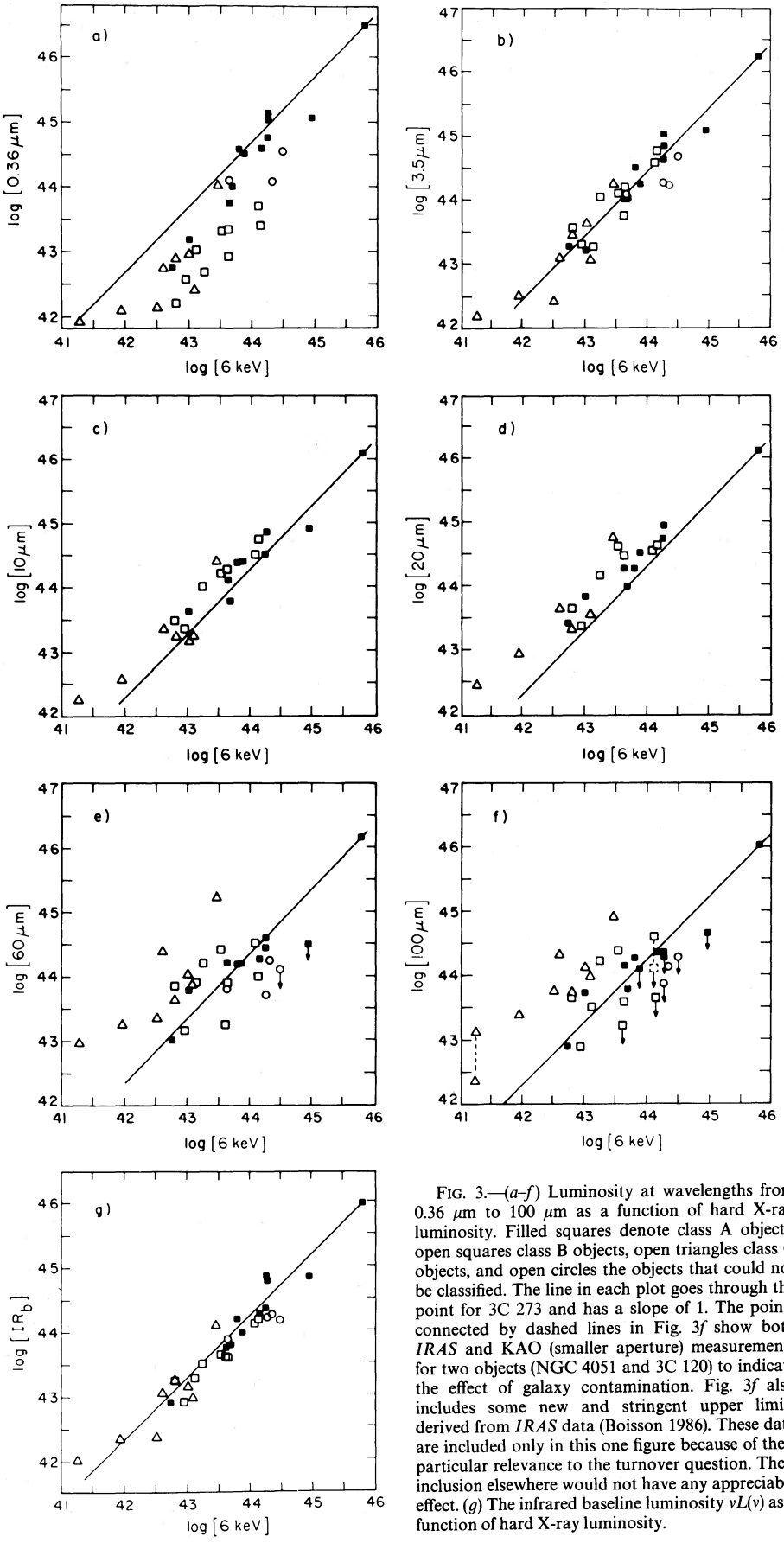

FIG. 3.—(*a–f*) Luminosity at wavelengths from 0.36 μm to 100 μm as a function of hard X-ray luminosity. Filled squares denote class A objects, open squares class B objects, open triangles class C objects, and open circles the objects that could not be classified. The line in each plot goes through the point for 3C 273 and has a slope of 1. The points connected by dashed lines in Fig. 3*f* show both *IRAS* and KAO (smaller aperture) measurements for two objects (NGC 4051 and 3C 120) to indicate the effect of galaxy contamination. Fig. 3*f* also includes some new and stringent upper limits derived from *IRAS* data (Boisson 1986). These data are included only in this one figure because of their particular relevance to the turnover question. Their inclusion elsewhere would not have any appreciable effect. (*g*) The infrared baseline luminosity $\nu L(\nu)$ as a function of hard X-ray luminosity.

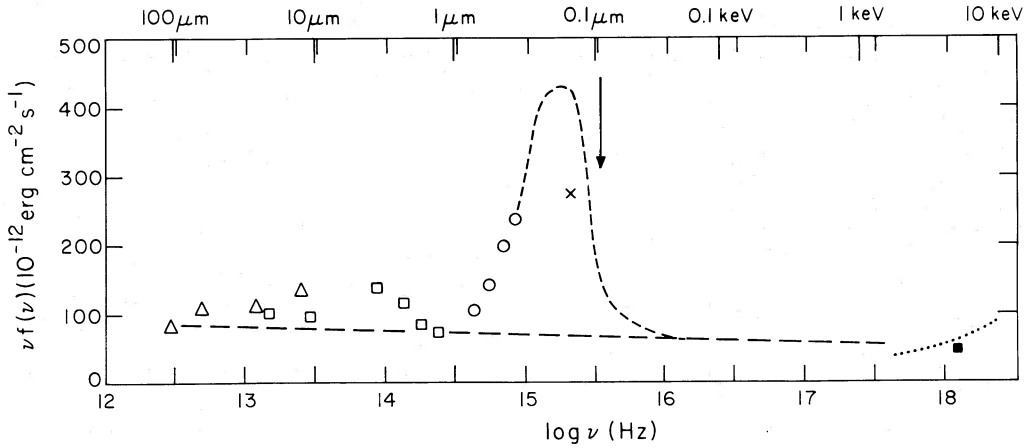

FIG. 4.—The energy distribution of 3C 273 plotted on a linear scale. Data points are as in Fig. 1 with the addition of the 6 keV point (*filled square*) from Piccinotti *et al.* (1982) and a point at 1450 Å from Véron-Cetty *et al.* The dotted line shows the X-ray spectral distribution measured by Worrall *et al.* (1979) on 1978 June 30. The difference between the two X-ray measurements probably represents source variability. The long-dashed line denotes the power-law baseline, and the short-dashed line represents a 27,000 K blackbody spectrum. The vertical arrow indicates the Lyman limit (912 Å).

estimate of its size. The big bump probably extends well beyond the Lyman limit and contributes a good share of the ionizing photons.

It is presumably an oversimplification to expect that all the central-source spectra are identical to that of 3C 273. In particular, Figure 3*e,f* shows that at 60 μm and 100 μm many objects have significantly less flux relative to X-rays than does 3C 273. We take this as evidence that the power-law component in their spectra is beginning to turn down, particularly as 3C 273 itself shows a slight but possibly significant downturn from 60 μm to 100 μm. A power-law turnover near 100 μm in some radio-quiet objects is not surprising, especially in comparison to radio-loud 3C 273. The confusion by galactic emission prevents any quantitative analysis of a possible turnover, however, and smaller aperture measurements in the 50–150 μm region would be very interesting in clarifying the matter. We emphasize that it is not simply a downturn between 20 μm and 60–100 μm that we take to be evidence for the beginning of a turnover in the power law, but rather the falling of the spectrum below the X-ray reference level. In our view, the downturn exhibited by many spectra is simply the low-frequency side of a blackbody curve that peaks near 20 μm. Edelson and Malkan (1986), lacking the X-ray reference, consider both possibilities. We believe that the availability of hard X-ray measurements is a strong aid in making a distinction, although good submillimeter data will resolve the matter directly.

III. EFFECTS OF DUST

a) Evidence for Reddening

The reddening indicated by the optical continuum slope [1.2 μm]/[0.36 μm] can be compared with two additional indicators of reddening: the line ratio [Hα]/[Hβ] and the "equivalent width" [6 keV]/*L*[Hα]. Paper I showed that all three indicators imply more reddening in the class B than in the class A nuclei. As the definition of the classes was based only on the first indicator, this is evidence that reddening is indeed the cause of the steeper optical slopes. Figure 5 compares the reddening values derived from each pair of indicators and shows that the reddening derived from the continuum slope is well-correlated with each of the other two measures. The predicted slopes derived from the reddening law of Savage and Mathis (1979) are also shown. Most of the observations agree reasonably well with the predictions, and the existence of a few objects that disagree is not surprising because Hα/Hβ is affected by radiative transfer (Kwan and Krolik 1981; Canfield and Puetter 1981) and [6 keV]/*L*[Hα] depends on both the covering factor of broad-line gas and the shape of the ionizing continuum between the Lyman limit and 6 keV.

A better measure of broad-line reddening might be obtained by using Paschen-alpha intensities in addition to Hα and Hβ (Carleton *et al.* 1984; Fabbiano *et al.* 1986). Unfortunately, Paα measurements are difficult for most of the objects in this low-redshift sample because the line lies in a region of strong atmospheric absorption. Lacy *et al.* (1982) used their observations of Paα, Hα, and Hβ to derive reddening values for the broad-line systems of six objects for our sample. These values correlate well with the continuum reddening that we infer from [1.2 μm]/[0.36 μm], but the subsample is too small to be significant.

b) Ultraviolet Energy Distributions

Although the ionizing ultraviolet spectrum cannot be observed directly, the optical and near-ultraviolet emission lines place lower limits on the flux of ionizing photons. These limits imply that the continua of class B objects are considerably reddened because the observed energy distributions do not furnish enough ultraviolet photons to generate the lines by photoionization. In the best-fitting "standard" photoionization model of Kwan and Krolik (1981), the assumed ionizing continuum is similar to the one shown in Figure 4, and the efficiency of hydrogen-line production is such that complete coverage of the central source by broad-line clouds would give *L*(Hα)/[912 Å] = 1/7. The observed ratio for 3C 273 is 1/44 based on simultaneous measurement of Hα and the near-ultraviolet continuum (Neugebauer *et al.* 1979) together with the relative values of *νf*(*ν*) at 3400 Å and the Lyman limit given by Malkan and Sargent (1982). The implied covering factor for 3C 273 is thus 15%.

Ultraviolet data exist for relatively few objects in our sample, and only a small fraction of the data are for class B objects. Véron-Cetty *et al.* compiled 1450 Å flux densities for Seyfert 1 galaxies from *IUE* data. From our sample, they list nine class A objects, including 3C 273, one class B object, 3C 120, and three class C objects. Boisson (1986) has provided us

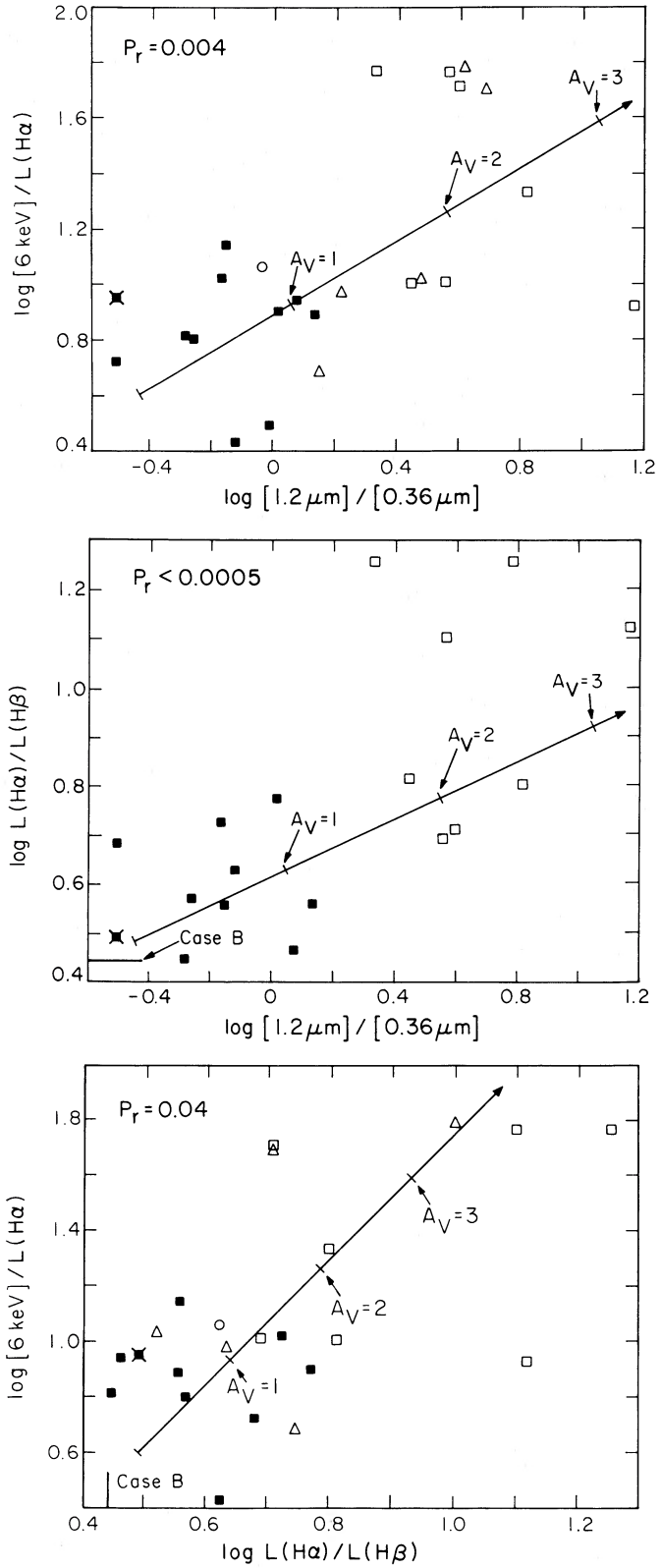

FIG. 5.—The correlations between three pairs of possible reddening indicators. Filled squares denote class A, open squares class B, and triangles class C objects; the starred point represents 3C 273. For each pair of reddening indicators, the significance P_r of the correlation given by the Spearman rank test is indicated. The arrows on each plot indicate reddening vectors based on the reddening law tabulated by Savage and Mathis (1979). The starting position of each arrow is arbitrary, so the arrows do not represent the regression line for the correlation. The lines on the Hα/Hβ axes indicate the case B ratio of Hα/Hβ.

with spectra of four additional class B objects, MCG 8-11-11, NGC 3227, MGC−6-30-15, and IC 4329A, and we have measured 1450 Å continuum flux densities from these. We have then computed covering factors from Hα fluxes and 1450 Å flux densities by assuming that all nuclei have the same slope as 3C 273 from 1450 Å through the ionizing continuum. The results for the class A and C nuclei range from 0.14 to 0.93. For four of the class B nuclei, however, the implied covering factors range from 1.3 to 5.3, and IC 4329A has a computed covering factor of 34. Unless there is an additional source of ionizing radiation that is undetectable at 1450 Å, these values certainly strain the capacities of photoionization models. It seems much more reasonable to assume that our line of sight to the ultraviolet continuum is affected by extinction, while the ionized gas sees the source more directly. The same conclusion holds for the remaining five class B objects, provided their spectra extrapolate from the *U* band to the Lyman limit in the same manner as the nuclei that have actually been observed.

The presence of a hard X-ray continuum does not appreciably help the problem of a lack of ionizing photons. High-energy photons are much less efficient at ionizing hydrogen than are photons with energy near the threshold. Kwan (1986) has shown explicitly that the line-production efficiency $L(\mathrm{H}\alpha)/[912\ \text{Å}]$ changes very little as the ultraviolet component of the spectrum is reduced relative to the X-rays. Thus to the extent that the observed ultraviolet flux densities indicate the behavior of the spectrum between 13.6 and ~30 eV, the higher energy photons do not affect the ionization.

c) *Dereddened Spectral Shape*

How would an increasingly reddened version of 3C 273 appear? The flux density near 1–2 μm would be little changed, but there would be a decrease in the blue and a thermal excess over the power law in the infrared. The shape of the infrared excess would depend on the distribution of dust and on the properties of the individual grains. If the dust were close-in and hot, the peak would come in the near-IR, and if the same kind of dust were farther out and cooler, the peak would appear at lower frequencies.

In the visible and near-infrared, a reddened 3C 273 spectrum is a reasonable representation of the observed spectrum of typical Seyfert 1 nuclei. Figure 6 shows the 3.5–0.36 μm portion of the median spectrum for class A objects normalized to the hard X-ray flux, together with the normalized spectrum of 3C 273. The effect of reddening the 3C 273 spectrum with $A_V = 0.24$ is also shown and is a reasonable fit to the median class A spectrum. The spectral shape of class B objects is poorly determined, because only one (NGC 931) has sufficient data to correct for starlight. Figure 6 shows that 3C 273 reddened by $A_V = 2.4$ is a reasonable fit to the spectrum of NGC 931. The other objects in class B are also reasonably fitted by a combination of reddened 3C 273 plus starlight, but accurate starlight subtraction is essential before this statement can be given strong weight. Rowan-Robinson and Crawford (1986) find their infrared-selected sample of Seyfert galaxies to have the same range of visual absorptions.

In spite of the reasonable fit to the data, it is most unlikely that a galactic reddening curve will correctly describe in detail the extinction to active galactic nuclei. For one thing, all of the dust is within our beam, so only absorption and not scattering contributes to the extinction. Therefore a larger dust column density is needed to produce the indicated values of A_V than for a Galactic source. Moreover, the shape of the reddening curve may differ from the Galactic reddening curve, because the albedo of the dust particles may depend on wavelength. We

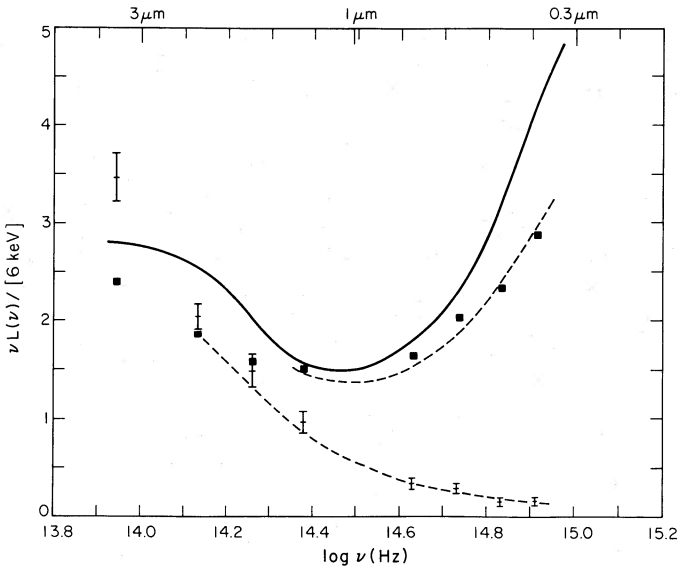

FIG. 6.—Comparison of observed Seyfert 1 energy distributions with the reddened energy distribution of 3C 273. The solid line is the observed 3C 273 spectrum shifted to the rest frame, while the two dashed lines show this spectrum with 0.24 and 2.4 mag of extinction (A_V). The squares represent the median energy distribution for class A nuclei normalized to the hard X-rays. The points represent the energy distribution of NGC 931, the only class B nucleus with starlight subtraction, normalized so the 3.5 μm flux density matches the median 3.5 μm flux density for all class B nuclei.

have used the Galactic reddening curve simply as a function that has a reasonable dependence on wavelength and for lack of any better option.

d) Thermal Emission

In order to test the hypothesis that energy is being absorbed in the visible and reradiated in the infrared, we compare the luminosities absorbed and reemitted. The amount of power potentially available in the thermal excess can be estimated by noting that dust efficiently absorbs energy between wavelengths of roughly 100 Å and 1 μm (log ν = 14.5–16.5) and emits between 1 and 100 μm (log ν = 12.5–14.5). Figure 4 shows that about 2.5 times as much power is available in the ultraviolet as is emitted by the power law in the infrared, so the thermal excess in the infrared could be more than twice the power under the infrared baseline. Table 1 give $L_{\rm below}$, the 1 to 100 μm luminosity below IR_b, and $L_{\rm above}$, the 1 to 100 μm luminosity above IR_b, for each object, and the ratio $L_{\rm above}/L_{\rm below}$ should approximate the ratio of thermal to nonthermal power for each object. Figure 7 shows the distribution of these ratios, and their range is just what we would predict: 0.7 ± 0.5 for class A and 2.0 ± 1.2 for class B. The higher ratio of 3.0 ± 1.4 for class C is consistent with a significant contribution from a galaxy disk and a relatively weaker nonthermal power law in these objects.

Figure 8 compares median spectra of classes A and B with that of 3C 273, which we have taken to represent the underlying spectrum. The singly hatched area in the infrared represents $L_{\rm above}$ for the class A median spectrum, and the similarly marked area in the ultraviolet represents a rough approximation to the power that might be absorbed by dust. The figure emphasizes how much energy 3C 273 emits in the ultraviolet and shows that even a small amount of reddening in the visible implies that a large amount of energy is being absorbed by the dust. Thus even objects with fairly blue energy distributions may have a strong infrared excess. Figure 8 also shows the additional infrared excess of class B objects as a doubly hatched area. The ultraviolet counterpart of this excess is the additional energy available for absorption because of heavier reddening. (The starlight included in the class B median spectrum is not important here.) An even more heavily reddened object could not convert a great deal more energy than the class B median, because there is not much more energy remaining at the wavelengths where the dust absorbs. Rowan-Robinson and Crawford (1986, Fig. 3*d*) have presented similar calculations that show more details of the spectral shape.

A good correlation between infrared excess and reddening will be generated if the amount of dust varies, but other parameters are constant. The scatter from the line of best correlation is a measure of the influence of patchiness or orientation. Figure 9*a*, *b* shows the dependence of $L_{\rm above}/L_{\rm below}$ on two reddening indicators. The correlation between thermal emission and reddening is strong, suggesting that we really are seeing the expected effects of dust in removing UV energy and reradiating it in the infrared. A possible complication is the relatively greater thermal emission of a galactic disk for low-luminosity nuclei. Figure 9*c* shows that there is indeed some luminosity dependence in the expected sense. However, this is not the major effect, as demonstrated by Figure 9*d*, which shows the same plot as Figure 9*a* but only for objects with log [6 keV] between 43.5 and 44.3. No luminosity effect on $L_{\rm above}/L_{\rm below}$ is observed in this range, as shown in Figure 9*c*. We consider these results persuasive evidence that an infrared excess accompanies reddening of the visible spectrum.

The smaller infrared excesses in high-luminosity objects are consistent with the conclusion of Lawrence and Elvis (1982) that dust content of AGNs decreases with increasing luminosity. The present result is less subject to selection biases as our sample is largely hard X-ray selected, and thus the selection of objects did not discriminate for or against dustiness *a priori*.

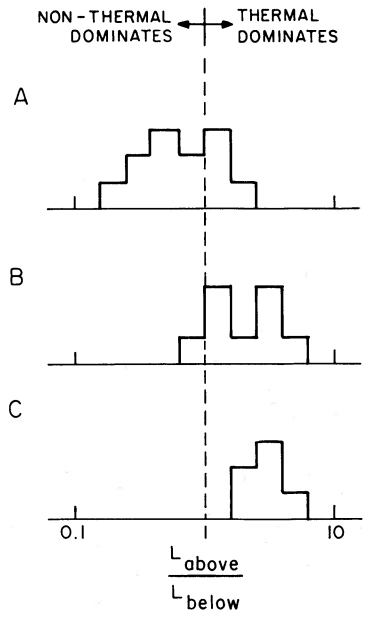

FIG. 7.—The distributions of the ratio of luminosities above and below the infrared baseline for class A, B, and C objects.

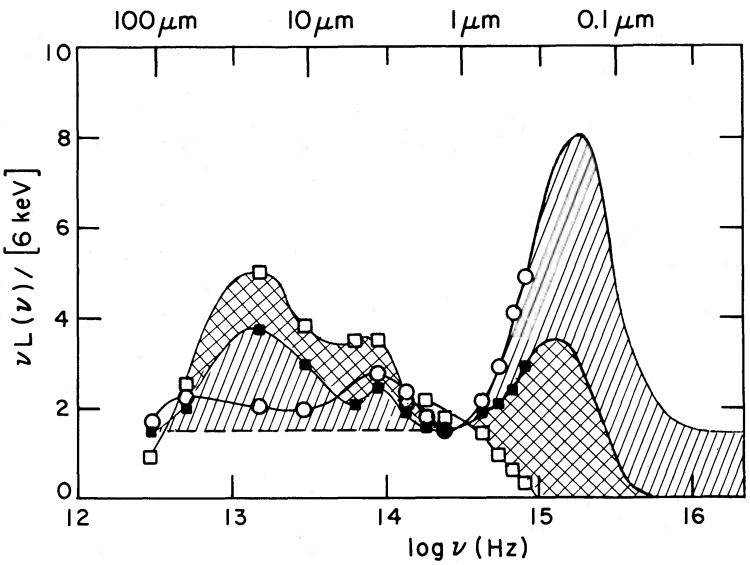

FIG. 8.—Comparison of the power inferred to be thermal emission with the power available in the ultraviolet. The circles represent the 3C 273 energy distribution, the filled squares the median energy distribution for class A objects, and the open squares the median energy distribution for class B objects. All energy distributions are normalized to the hard X-rays. Single hatching shows the ultraviolet power hypothesized to be absorbed by dust and the infrared power reradiated by dust for the median class A object. Double hatching indicates the extra power absorbed and reemitted for the median class B object.

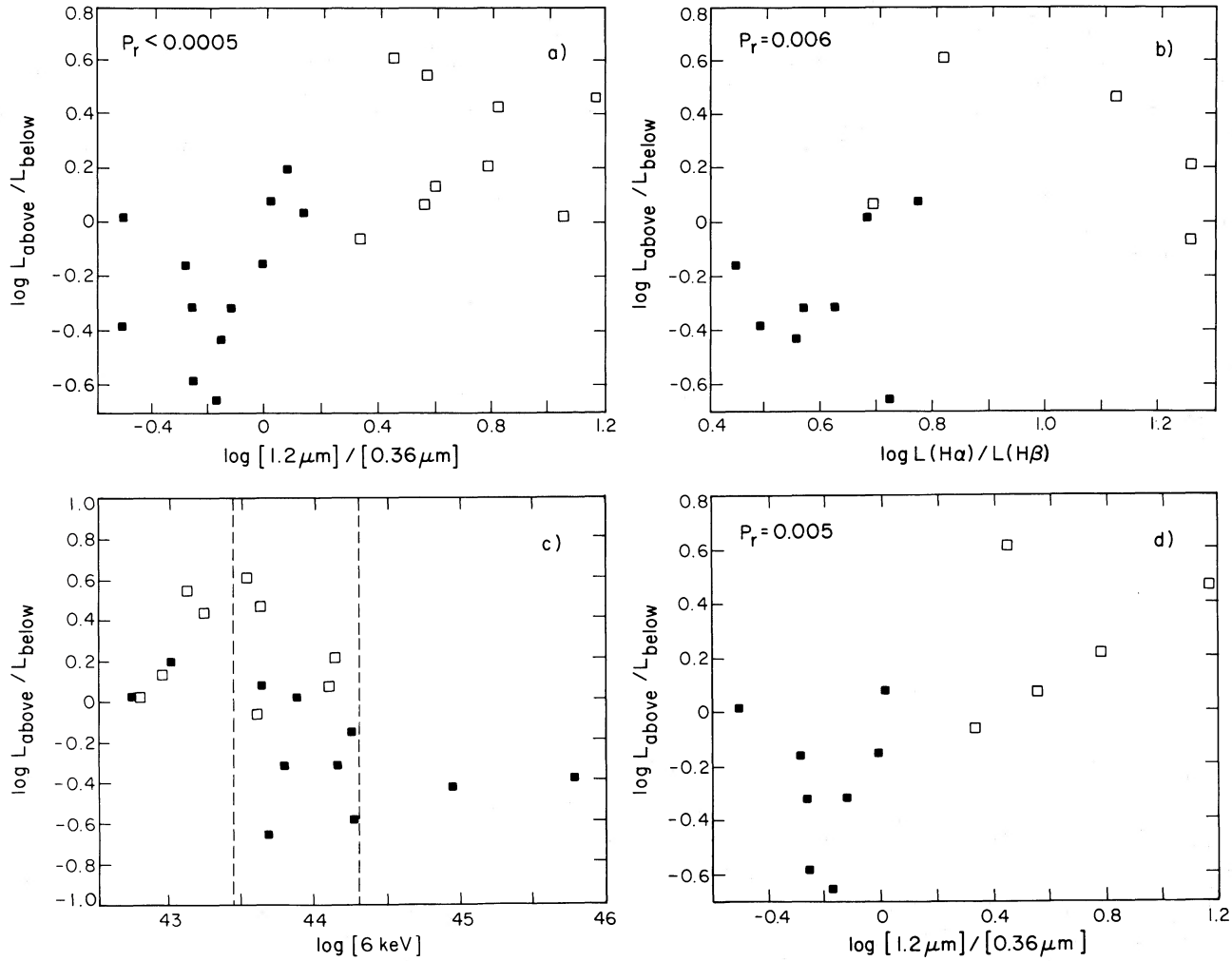

FIG. 9.—(*a*, *b*) The correlation of the ratio of infrared luminosity above and below the power-law baseline with two reddening indicators. Filled squares denote class A and open squares class B objects. (*c*) Dependence of the ratio of luminosity above and below the power-law baseline on the 6 keV luminosity. (*d*) Same as (*a*) but only for objects with log [6 keV] between 43.5 and 44.3, i.e., objects between the vertical dashed lines in (*c*). The correlation shown in (*a*) is not spoiled by restricting the sample to a small range of luminosity. The significance P_r of each correlation as measured by the Spearman rank test is given in the appropriate diagram.

The sample is small, however, and so contains few of the rare radio-loud AGN. Among radio-selected objects, some strongly reddened high-luminosity cases certainly exist (e.g., 3C 234—Carleton *et al.* 1984).

e) Radial Distribution of Dust

So far we have treated only the integrated luminosity of the thermal infrared emission, but of course the energy distribution depends upon the temperature distribution of the emitting dust. The dust temperature depends on both the distance of the absorbing clouds from the heating source and on necessarily uncertain dust properties. A very simple expression given by Davidson and Netzer (1979),

$$T \approx 1 \times 10^{-6}(L_{\rm eff}/r^2)^{1/5}\ , \qquad (1)$$

agrees reasonably well with more extensive calculations (e.g., Rees *et al.* 1969; Rudy and Puetter 1982). In equation (1), T is the dust temperature in kelvins, $L_{\rm eff}$ is the effective luminosity of the heating source in ergs s^{-1}, and r is the distance in pc of the dust from the source. The T^5 dependence instead of T^4 occurs because the emissivity of the dust was assumed to vary as λ^{-1}. As noted in § III*d*, the effective power for heating dust might be up to 2.5 times $L_{\rm below}$. The median value of $L_{\rm below}$ for class A and B objects is about 2×10^{44} erg s^{-1}, and therefore 5×10^{44} ergs s^{-1} is a typical value for $L_{\rm eff}$. Using this value, the observed emission at 3.5, 20, and 80 μm must typically arise at distances of r(1000 K) $\approx$ 0.7 pc, r(180 K) $\approx$ 50 pc, and r(45 K) $\approx$ 1600 pc. Cool dust may also exist close in, of course, if it is in the shadow of dust or gas that is still closer to the center. The smallest radius above is comparable to the size of 0.1–0.3 pc for the broad-line region inferred from the calculations of Kwan and Krolik (1981) together with the luminosity assumed above. Calculations for the size of the narrow-line region (Ferland 1981) and the same luminosity give a radius of 30–300 pc, corresponding to the second temperature and radius above. The third temperature and radius correspond to the inner part of a galactic disk.

Many objects show a pronounced bump in the spectrum at 3.5 μm. This bump has been previously noted for NGC 4151 (Rieke and Lebofsky 1981) and even occurs in 3C 273 (Neugebauer *et al.* 1979). The 3.5 μm peak is very well defined in class A objects, where the excess emission nearly always decreases from 3.5 μm to 5 or 10 μm. Its amplitude in the 3C 273 spectrum (relative to [IR_b]) is 0.27 in log $vf(v)$, while the average over the entire sample is 0.29 ± 0.19. The dispersion in the ratio log ([3.5 μm]/[6 keV]) is 0.27, while the dispersion in log ([IR_b]/[6 keV]) = 0.23. Thus the data are consistent with the infrared baseline and the 3.5 μm bump being independent components. Direct evidence that these components are separate has been seen in 3C 273, where variations that occurred on a time scale $\sim$1 month were of smaller amplitude at 2.3 and 3.5 μm than at other wavelengths (Cutri *et al.* 1985; Robson *et al.* 1983).

If the 3.5 μm bump is due to dust, a significant fraction of central-source radiation is intercepted very close in, at $r \approx 0.5$ pc. One possible alternative explanation is that the 3.5 μm peak is not radiation from hot dust but from the ionized gas. Puetter and Hubbard (1985) showed that the gas responsible for the broad emission lines could generate considerable free-free emission in the 3 μm neighborhood if the density were as high as 10^{11} cm^{-3}. The problem with this as an explanation for the 3.5 μm bump is that the free-free emission is not very sharply peaked. Figure 10 shows that a single blackbody curve gives a much better fit to the short wavelength side of the bump in the 3C 273 spectrum than does free-free radiation.

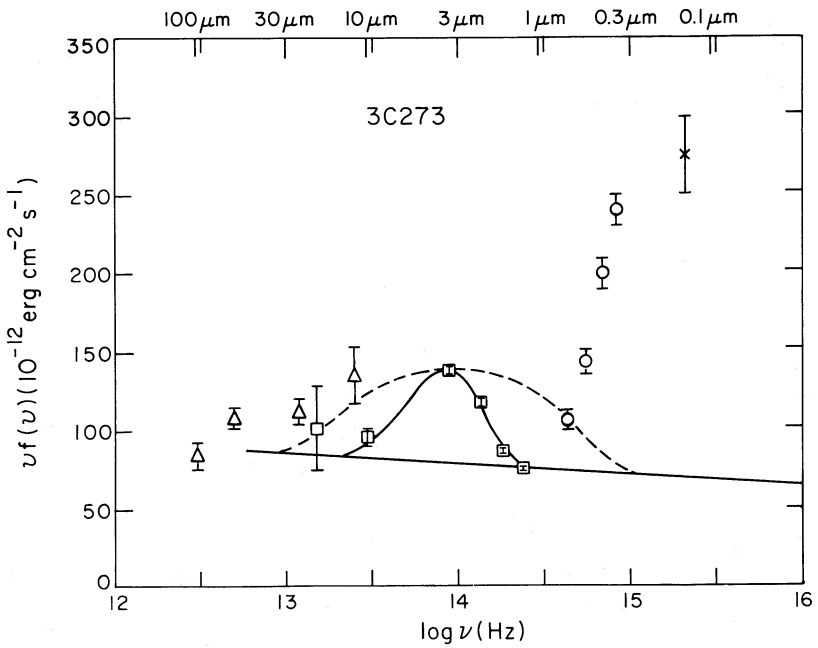

FIG. 10.—The 3C 273 energy distribution near 3.5 μm plotted linearly. Triangles denote *IRAS* data, squares denote ground-based infrared data, circles denote *UBVR* photometry, and the cross is a point at 1450 Å from Véron-Cetty *et al.* The solid lines show a power law and a single blackbody curve at 1050 K. The dashed line shows a possible free-free contribution from dense ionized gas (Fig. 1*a*, curve 2 of Puetter and Hubbard [1985]).

A test of whether the 3.5 μm bump is due to dust is to compare the excess 3.5 μm emission with the amount of reddening. The result for two reddening indicators is shown in Figure 11*a*, *b*. There is certainly considerable scatter, but a general increasing trend is evident. This result is consistent with the suggestion that the 3.5 μm bump could be emission from dust in or near the broad-line region.

The median spectra in Figure 8 show that the largest infrared excesses occur at wavelengths of 10 to 25 μm. These wavelengths imply that the radiating dust lies mostly at $r \approx 50$ pc if the dust is directly exposed to the central source or closer if most of the dust is shadowed. The relative amounts of emission and absorption indicated in Figure 9 imply that the covering factor of this dust must be quite substantial in some cases, including most of the class B objects. The implied covering factor would be reduced only if the intrinsic source spectra have big bumps even larger than that of 3C 273. Figure 11*c–f* shows the correlation of 10 and 20 μm excesses with reddening. The 10 μm excess correlates surprisingly well with Balmer decrement (Fig. 11*d*), implying that the dust radiating at 10 μm is the same dust that reddens the broad emission lines. The other correlations are poorer, but the trends are in the right direction. The scatter in these diagrams may be assigned either to random patchiness or to systematic orientation effects. In either case, the amount of dust in our line of sight is not necessarily proportional to the amount of dust surrounding the object.

Finally, the median spectra do not show much excess emission at 60 to 100 μm, suggesting that no appreciable amount of the energy is intercepted at distances in the kiloparsec range. Such dust would, of course, appear the same as galactic disk emission, and the objects with much dust in this range would be placed in class C. Nevertheless, only a small fraction of the original sample was in class C, and Paper I gave evidence that most of the emission from these came from galactic disks (which may include bursts of star formation) rather than from nuclei.

If dust in AGNs is actually concentrated with the gas at two separate distances, the expected dust temperatures at the distances of the broad-line gas and the narrow-line gas suggest that there should be a close connection between Hα and 3.5 μm emission and between [O III] and, say, 20 μm. This is in agreement with our correlation analysis (Tables 3 and 4; Fig. 13*b*, *c*), which shows that [3.5 μm] correlates better with L(Hα) than with L([O III]), while [20 μm] correlates better with L([O III]). It is too much to expect [O III] and [20 μm] or Hα and [3.5 μm] to be uniquely correlated, because differences in the gas-to-dust ratios or in the relative efficiency of dust heating and ionization would add considerable scatter to the relation. If, however, one forms a second ratio that is independent of these effects, the scatter is much reduced. Figure 12 illustrates this, showing that as the narrow-line region becomes more dominant, (i.e., high [O III]/Hα), the cooler dust emission grows relative to the hot dust emission (i.e., high [20 μm]/[3.5 μm]). The total "thermal luminosity," $L_{\rm above}$, is less well linked with L([O III]) than is [20 μm]. This simply reflects the fact that $L_{\rm above}$ integrates emission from dust covering a factor of $\sim$30 in temperature. This dust must be physically spread by factors of $\sim$ 5000 in radius if the central source is the only heat source.

IV. COMPARISON WITH OTHER MODELS

Our analysis of the continua of Seyfert 1 nuclei is unique in that we postulate a universal ν^{-1} power-law continuum in the infrared and ascribe all departures from it to the effects of dust. The dust hypothesis explains all the data with a single type of central source, scaled only in luminosity, and a single additional physical process: the absorption of radiation by dust and subsequent thermal reradiation. A different approach has been taken by EM, who try to explain the 0.1–100 μm continuum of objects such as these with minimal recourse to the effects of dust. They postulate a power-law component with a variable slope plus additional components with variable amplitudes to account for the continuum radiation. A comparison with their work is a good means of summarizing our analysis with emphasis on the features that are particular to it.

One difficulty with the EM interpretation of the infrared continuum is that it does not predict the good correlation between [3.5 μm] and [6 keV]. As each spectrum has a different slope, the 3.5 μm luminosity represents a different sampling of the bolometric luminosity in the power law in each galaxy, unless for some reason the power-law "pivots" about the 3.5 μm point. By contrast, in our picture where a power law of fixed slope underlies the infrared spectrum, any point on the power law equally well represents the luminosity in that component. The only special property of the 3.5 μm point is that it is little contaminated by other components (nuclear dust, starlight, cool dust in the galaxy disk). The lowest $\nu L(\nu)$ point, being a better representation of the power law, correlates even better with hard X-rays.

The dust hypothesis and the EM hypothesis of diverse continua have two differences that are directly testable. Those are the amount of reddening and whether the infrared emission is thermal or nonthermal. Statistical tests to distinguish between the different infrared emission mechanisms have been discussed above, and we discuss possible direct tests below. We have suggested that the objects in class B have reddening corresponding to $A_V \geq 2$, while EM derive $A_V = 0.3$ for 3C 120, the only one of our class B objects in their sample, and similar values for other Seyfert 1's and QSOs with steep spectra.

The reddening can be measured most easily from the emission lines, but it is really the continuum reddening that must be determined. Although there is certainly evidence of line and continuum reddening at the few tenths magnitude level required by EM (MacAlpine 1985; EM), there is also evidence of larger reddening in some objects ($A_V \sim 1.5$, Lacy *et al.* 1982; Fabbiano *et al.* 1986; Carleton *et al.* 1984; this work, §§ III*a* and III*b*). Moreover, the samples studied by MacAlpine and EM are probably biased toward low reddening (e.g., Rudy 1984).

There is a fundamental difficulty with any assertion that the infrared emission is entirely nonthermal, with no thermal emission from dust at all. Even the modest amounts of visual absorption generally conceded to be present (e.g., the median $A_V \approx 0.2$ found by EM) imply that more than half of the energy emitted in the ultraviolet should be absorbed by dust and reemitted somewhere in the infrared. Unless the absorption occurs at a very large distance from the nucleus, dust must make a considerable contribution to the infrared emission. If absorption and thermal emission is found even in samples biased against dust content (Rudy 1984), it must be even more important in unbiased samples.

The most direct evidence for dust emission would be the detection of dust spectral features in emission. Searches so far have had little success (e.g., Roche *et al.* 1984; Aitken and Roche 1985; Moorwood 1986). However, failure to detect fea-

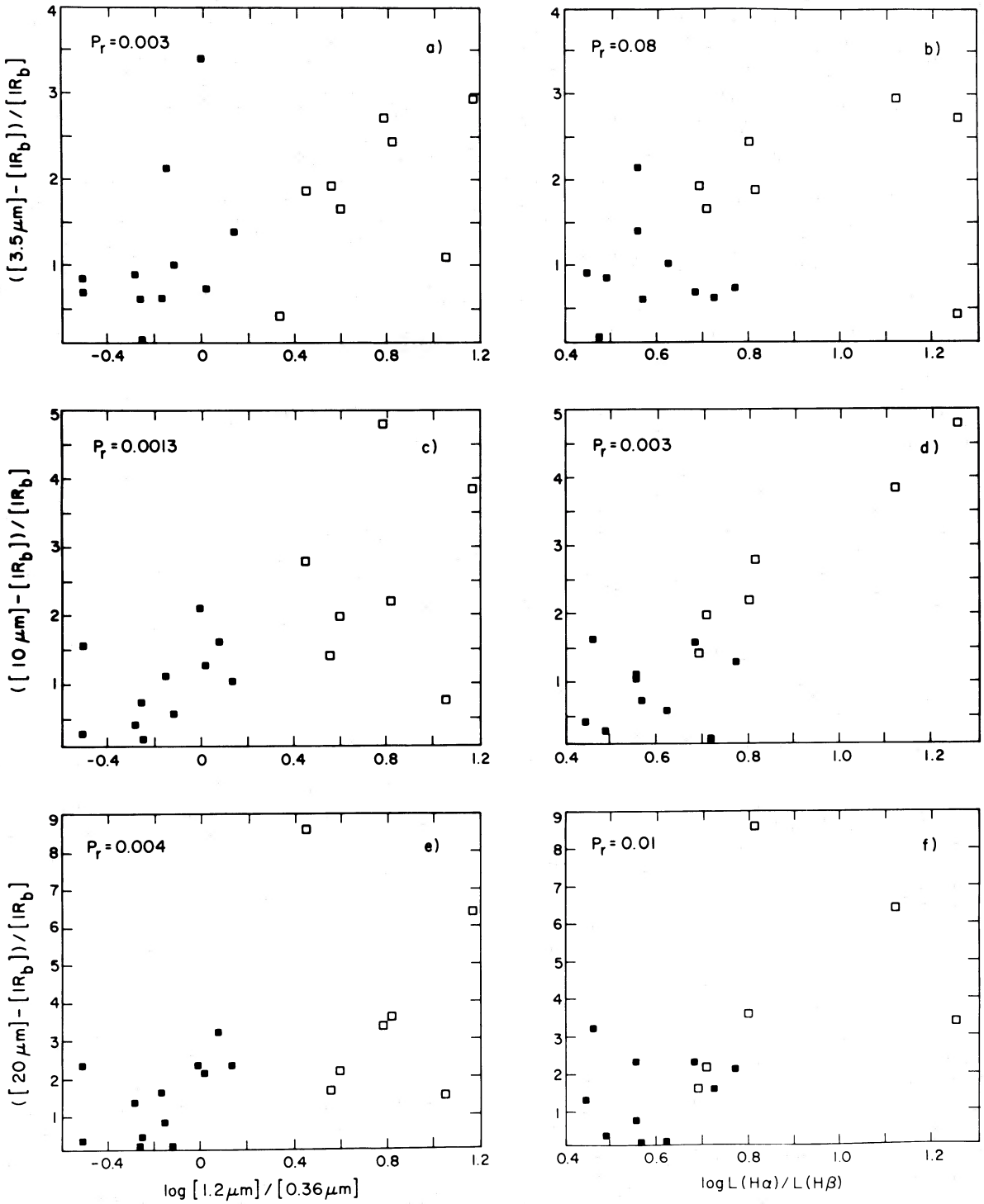

FIG. 11.—Ratio of luminosities above and below the power-law baseline at individual wavelengths correlated with two reddening indicators. Filled squares denote class A and open squares class B objects. The quantity plotted is hypothesized to represent the ratio of thermal to nonthermal luminosity at each wavelength. The probabilities P_r that the correlations could arise by chance (based on a Spearman rank test) are given in each frame. (*a*, *b*)–3.5 μm; (*c*, *d*)–10 μm; (*e*,*f*)–20 μm.

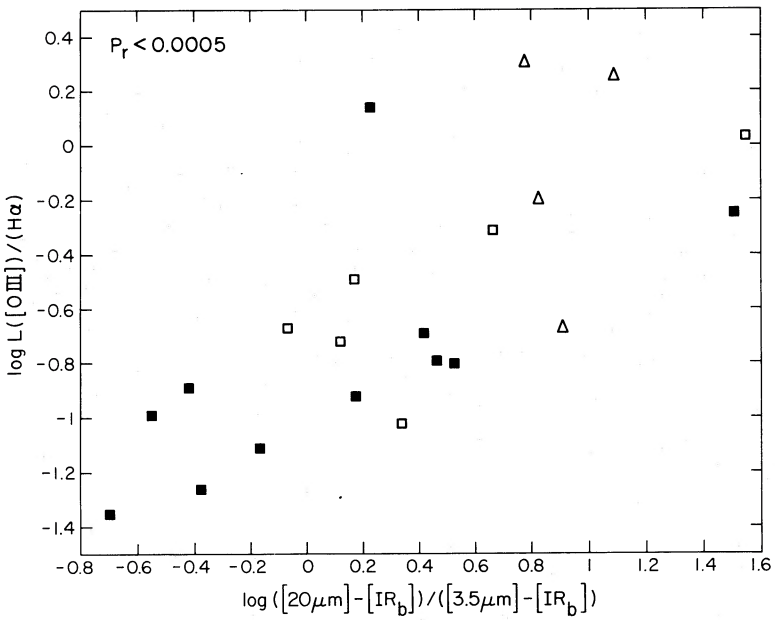

FIG. 12.—Correlation of the ratio of narrow to broad emission lines with the ratio of infrared excesses due to dust inferred to be at the distances of the narrow and broad emission-line regions. The dust contributions are taken to be the excesses above the infrared baseline at 3.5 and 20 μm, respectively. Solid squares denote class A objects, open squares denote class B objects, and triangles denote class C objects. The correlation significance is indicated.

tures counts only very weakly against a thermal origin for a good fraction of the infrared continuum, as these features depend strongly on dust properties which may well be very different in active nuclei. Large grain sizes, thick mantles, optically thick clouds, or less silicate rich grains would all weaken the dust features. Indeed, Seyfert 2 nuclei generally show smooth spectra, and none shows silicate emission, in spite of the fact that those nuclei are generally considered to be dominated by dust emission (Rieke 1985; EM).

Other tests to distinguish thermal from nonthermal emission include the presence and character of variability (Rees *et al.* 1969), polarimetry, and measurement of source size. Most existing observations of variability (Lebofsky and Rieke 1980; Rieke and Lebofsky 1979, 1981; Cutri *et al.* 1985) favor thermal emission, but there are too few observations for a definitive test. Multiwavelength polarization studies are also consistent with thermal emission but far from conclusive (Rudy *et al.* 1982). Direct measurement of source sizes in the infrared is not yet practical but very soon will become so.

V. CONCLUSIONS

We suggest that the continua of Seyfert 1 nuclei may be understood as a single underlying spectrum similar to the observed spectrum of 3C 273 together with dust absorption and thermal reemission. While the underlying nonthermal continua undoubtedly differ in some degree, the assumption of a single spectrum is consistent with all of the data for our hard X-ray emitting sample. The dust hypothesis explains numerous relations among the observed quantities in a simple, physically plausible way. We deduce a continuum reddening corresponding to $A_V \approx 2$ for the objects with the steepest optical spectra. It would be interesting to examine other samples that are weaker in hard X-rays to see if the same interpretation is viable.

If the picture of identical central sources with different dust contributions is correct, most of the absorption of central source radiation and thermal reemission by dust takes place at distances corresponding to the region where the narrow emission lines are formed. There is also an emission component that can be understood as dust at distances typical of the broad-line region. Most infrared wavelengths contain some contribution from dust emission, and the most reliable windows to the central nonthermal continuum are between 1 and 2 μm and at wavelengths longer than 100 μm. These are unfortunately just the regions where the host galaxy has large contributions from starlight and from cool dust. This emphasizes the necessity of subtracting starlight from observations made in the visible and near-infrared. Small beam observations in the far-infrared and submillimeter regions would be extremely valuable, though difficult to obtain.

There are several areas of future work suggested by our explanation of the infrared and visible continua.

1. Monitor variability of steep-spectrum objects at 10–20 μm and shorter wavelengths simultaneously. To the extent that this has been done, evidence favors our model.

2. Investigate whether the observed details of the 8–13 μm spectrum can be reproduced with some reasonable combination of dust composition, temperature distribution, and optical depth. As we are uncertain about the range of "reasonable" dust composition and about the geometry, this approach may not yield a clear distinction between hypotheses.

3. Construct emission-line models to compare the effects of the reduced ultraviolet fluxes implied by the steep continuum hypothesis with the much larger fluxes implied by the reddening hypothesis.

4. Obtain high-resolution images at 10 and 20 μm. If the emission is nonthermal, the nuclei should be very small, while thermal emission should come from regions of order 100 pc in diameter. Comparison of infrared and emission-line images should indicate whether dust is directly associated with line-emitting gas.

5. Obtain smaller aperture far-infrared and submillimeter observations so as to define better the possible turnover region of the nonthermal spectrum. This would assist in separating thermal and nonthermal components in this region and in modeling the generation of the X-ray spectrum.

The authors thank C. Boisson for communicating data in advance of publication, E. H. Avrett for valuable discussions, and A. W. Campbell for helpful comments on the manuscript.

This paper and its companion depend strongly upon the extensive, high-quality observational work of Dr. Christopher W. McAlary, with whom we have had many interesting and useful conversations. Dr. McAlary's untimely death, with his work in astrophysics only just begun, has taken from us a colleague whom we greatly valued for his intellect and for his brightness and good cheer.

APPENDIX

CONTINUUM AND EMISSION-LINE CORRELATION

We present here a formal analysis of correlations between some of the line and continuum luminosities for the objects in our sample. To keep the amount of information manageable, we will use the following data.

1. [6 keV], to represent the central source continuum.
2. $L(\mathrm{H}\alpha)$, to represent gas in the broad-line region.[3]
3. $L([\mathrm{O\ III}])$, to represent gas in the larger forbidden-line region.
4. [20 μm], to represent the infrared region most likely to be contaminated by warm-dust emission.
5. [3.5 μm], to represent the same for hot-dust emission.
6. [IR_b], (the lowest point in the 1.2–100 μm range) to represent a possible infrared "window" on the central-source continuum.
7. L_{above}, (discussed in § III*b*) to represent a possible measure of thermal dust emission above the infrared baseline [IR_b].

Table 2 gives a compilation of all the continuum and emission-line luminosities used in the correlation analysis. Table 3 gives the

[3] For broad-line objects, this is the luminosity in the broad component. For the narrow-line galaxies NGC 2992 and NGC 5506, the total Hα luminosity was used.

TABLE 2

CONTINUUM AND LINE LUMINOSITIES USED IN CORRELATION ANALYSIS

Object	[6 keV]	[3.5μm]	[20μm]	[IR_b]	L(Hα)	L([OIII])	(ref)
Class A:							
III Zw 2	44.95	45.03	-	44.83	43.81	42.92	(a)
F-9	44.26	44.99	-	44.85	43.77	42.56	(a)
Akn 120	43.80	44.46	44.25	44.18	43.37	42.02	(a)
Mkn 79	43.64	44.04	44.24	43.75	42.74	41.95	(a)
NGC 3783	43.01	43.64	43.82	43.20	42.07	41.82	(a)
NGC 4151	42.74	43.14	43.39	42.89	41.85	41.86	(h)
3C273	45.79	46.15	46.04	45.97	44.84	43.58	(b)
NGC 5548	43.69	43.96	43.97	43.78	42.67	41.98	(a)
Mkn 1383	44.27	-	-	44.78	-	-	-
Mkn 841	43.88	44.21	44.49	43.98	43.16	42.36	(a)
ESO 141-G55	44.16	44.51	-	44.27	43.36	42.37	(a)
Mkn 509	44.25	44.60	44.72	44.35	43.44	42.52	(a)
Class B:							
NGC 526a	43.61	43.73	-	43.60	41.84	41.74	(c)
NGC 931	43.24	44.01	44.16	43.50	41.91	41.42	(c)
3C120	44.10	44.55	44.52	44.12	43.09	42.43	(a)
MCG-8-11-11	43.53	44.06	44.60	43.63	42.53	42.22	(a)
3A 0557-385	44.14	44.74	44.58	44.18	-	-	-
MCG-6-30-15	42.95	43.29	43.39	42.90	41.24	40.52	(a)
IC 4329A	43.63	44.24	44.45	43.59	42.71	41.69	(a)
NGC 5506	42.79	43.47	43.53	43.23	40.73	40.92	(e)
ESO 103-G35	43.12	43.25	-	43.27	41.36	41.39	(f)
Class C:							
NGC 2992	43.09	43.04	43.54	42.97	41.31	41.56	(g)
NGC 3227	41.95	42.45	42.94	42.33	40.25	40.55	(a)
NGC 4051	41.27	42.18	42.46	42.01	40.30	40.10	(a)
NGC 4593	42.80	43.42	43.30	43.23	41.78	40.88	(a)
NGC 7172	43.01	43.59	-	43.16	-	-	-
NGC 7213	42.48	43.17	-	43.11	41.3	40.78	(d)
NGC 7314	42.51	42.41	-	42.36	-	-	-
NGC 7469	43.46	44.22	44.72	44.08	42.78	42.11	(a)

References for Hα and [O III]: (*a*) Rudy 1984; (*b*) Neugebauer *et al.* 1979; (*c*) Ward (unpublished data); (*d*) Phillips 1979; (*e*) Wilson *et al.* 1976; (*f*) Phillips *et al.* 1979; (*g*) Ward *et al.* 1980; (*h*) Yee 1980.

TABLE 3

SPEARMAN RANK CORRELATION RESULTS[a]

	[6 keV]	[3.5μm]	[20μm]	[IR_b]	L_{above}	L(Hα)	L([O III])
[6 keV]	N[b] r[b] p[b]	20 0.946 <5x10^{-7}	15 0.854 ~5x10^{-5}	21 0.981 <<5x10^{-7}	18 0.752 ~7x10^{-5}	19 0.858 <5x10^{-7}	19 0.940 ~8x10^{-7}
[3.5μm]	11 0.982 <5x10^{-7}	---	15 0.924 <5x10^{-7}	20 0.936 <5x10^{-7}	18 0.884 <1x10^{-6}	19 0.937 <5x10^{-7}	19 0.840 ~1x10^{-6}
[20μm]	8 0.976 ≈5x10^{-6}	8 0.976 ~5x10^{-6}	---	13 0.846 ~5x10^{-5}	15 0.955 <5x10^{-7}	14 0.836 ~1x10^{-5}	14 0.801 ~2x10^{-4}
[IR_b]	12 0.972 <5x10^{-7}	11 0.982 <5x10^{-7}	8 0.952 ~8x10^{-5}	---	18 0.741 ~2x10^{-4}	19 0.928 <5x10^{-7}	19 0.861 ~5x10^{-7}
L_{above}	9 0.933 ~8x10^{-4}	9 0.952 ~7x10^{-5}	8 0.976 ~5x10^{-6}	9 0.900 ~8x10^{-4}	---	17 0.709 ~5x10^{-4}	17 0.666 ~2x10^{-3}
L(Hα)	11 0.964 ~5x10^{-7}	11 0.991 <<5x10^{-7}	8 0.976 ~5x10^{-6}	11 0.973 <5x10^{-7}	9 0.917 ~4x10^{-4}	---	19 0.902 <5x10^{-7}
L([O III])	11 0.936 ~7x10^{-6}	11 0.909 ~7x10^{-5}	8 0.833 8x10^{-3}	11 0.909 ~7x10^{-5}	9 0.850 2x10^{-3}	11 0.900 ~8x10^{-6}	---

[a] Quantities to upper right of diagonal are for class A and B objects, while quantities to lower left are for class A only.

[b] Values in table are the number of objects N, the correlation coefficient r, and the probability P that random observations would show a correlation coefficient as high as r.

results from performing a nonparametric Spearman rank correlation test on all the pairs of variables. For each correlation, the one-tailed probability that the correlation might arise by chance is given in the first line, the correlation coefficients in the second line, and the number of objects in the third line.

The observed correlations are not likely to be due to a selection bias. Although our sample is flux-limited in the X-rays, all galaxies were observed and detected at 3.5 μm. As flux was not an *a priori* selection at this frequency, we can exclude the possibility that the 3.5 μm to X-ray correlation results from a distance bias. The same is true for the correlations with the line luminosities, which are available for most of the galaxies in the sample. The presence of a dominant distance bias in the correlations with the 20 μm luminosity is therefore also unlikely. Moreover the correlations are also present, although to a lesser degree, in the relationships between the fluxes.

Having established correlations of infrared with other emission parameters, we raise the question: which, if any, of these correlations are intrinsically valid, and which may be the secondary results of other primary correlations? These questions can be answered with the Spearman partial rank correlation test (Kendall and Stuart 1979; for previous applications of this test in astrophysics see Macklin 1982; Tananbaum *et al.* 1983; Fabbiano *et al.* 1984; and Fabbiano and Trinchieri 1985). The test gives partial correlation coefficients, which represent the conditional probabilities of correlations between two variables in a group of three or more when the other variables are kept fixed. We have applied this test to groups of three or four variables both for the entire sample and for the sample obtained by excluding the "galaxy dominated" class C galaxies. (See Paper I.) We have not applied this test to class A galaxies alone because the number of objects detected in all the variables is generally too small. Table 4 lists the resulting probabilities, and the relations among some of the variables are shown graphically in Figure 13. Given the intrinsic nature of partial correlation analysis (see Kendall and Stuart 1979), the confidence of a correlation between two variables depends upon the set of variables chosen, as for any choice of variables it is always possible that the correlations under examination are a consequence of a link with some variable not considered. This explains, for example, why the formal conditional probability of a link between L([O III]) and [20 μm] is different when this correlation is tested relative to the L(Hα) and [3.5 μm] variables or relative to the L_{above} variable.

One result of our correlation analysis is the lack of a strong connection between [6 keV] and L([O III]) (Fig. 13*d*). In a picture where all the emission lines arise from photoionization by the central UV/X-ray source, a strong and direct correlation of L([O III]) with [6 keV] is expected. The lack of such a correlation suggests that variation of covering factor and variations in the far UV/soft X-ray continuum (between 912 Å and 6 keV) are important.

TABLE 4

SPEARMAN RANK PARTIAL CORRELATION RESULTS

Values Correlated	All Objects ρ^a	All Objects Pb	Class A and B only ρ^a	Class A and B only Pb
a: [6 keV], [3.5μm], [IR_b]				
	(28 objects)		(20 objects)	
[6 keV], [3.5μm]	0.257	0.099	0.404	0.045
[3.5μm], [IR_b]	0.600	<0.005	0.115	0.320
[IR_b], [6 keV]	0.587	<0.005	0.846	<0.005
b: L(Hα), L([O III]), [20μm], [3.5μm]				
	(19 objects)		(14 objects)	
L(Hα), L([OIII]	0.625	<0.005	0.641	0.013
L(Hα), [20μm]	-0.244	0.195	-0.480	0.059
L(Hα), [3.5μm]	0.721	<0.005	0.782	<0.005
L([OIII]), [20μm]	0.564	0.009	0.596	0.022
L([OIII]), [3.5μm]	-0.426	0.045	-0.505	0.048
[20μm], [3.5μm]	0.684	<0.005	0.840	<0.005
c: L[O III], [20μm], L_{above}				
	(18 objects)		(14 objects)	
L([OIII]), [20μm]	0.741	<0.005	0.763	<0.005
[20μm], L_{above}	0.947	<0.005	0.953	<0.005
L_{above}, L([OIII])	-0.534	0.015	-0.596	0.017
d: [6 keV], L(Hα), L([O III])				
	(25 objects)		(19 objects)	
[6 keV], L(Hα)	0.654	<0.005	0.749	<0.005
L(Hα), L([OIII])	0.648	<0.005	0.545	0.010
L([OIII]), [6 keV]	0.087	0.345	0.069	0.394

[a] Correlation coefficient.

[b] Probability of random data being this well-correlated.

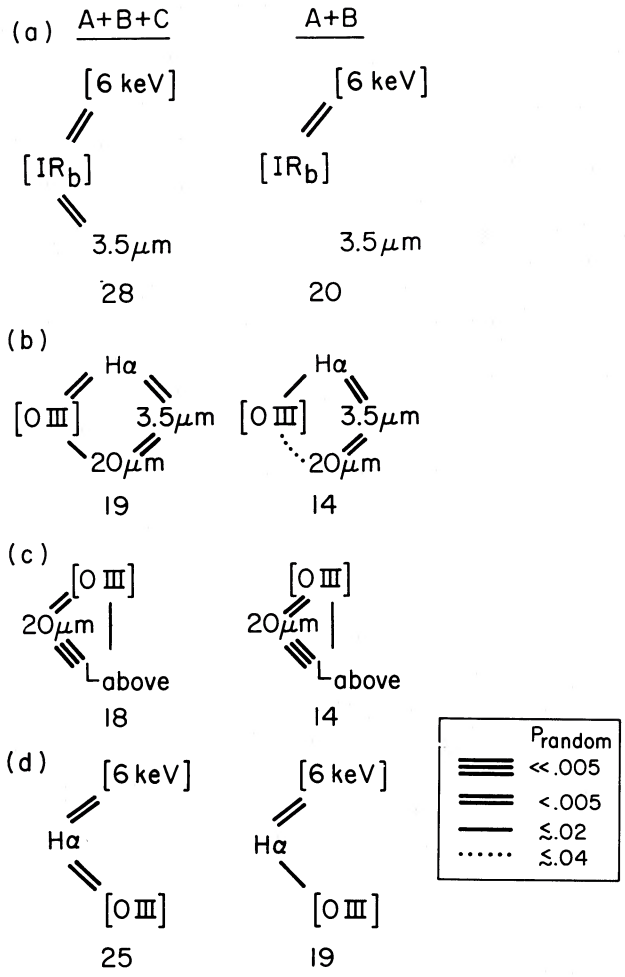

FIG. 13.—Summary of the results of the Spearman partial rank correlation test (Table 4). The left column is for all objects, while the right column includes class A and B objects only. The results indicate the conditional probability of correlation between any two variables in a group of three or more when the others are kept fixed. Quantities connected by multiple lines are the most closely related, and these relations are taken to be intrinsically significant. The formal probabilities associated with each marking are given in the legend and range from $P_{random} \ll 0.005$ for a triple line to $P_{random} \leq 4\%$ for a dotted line; absence of a line indicates that the correlation is insignificant. The number of objects included in each test is written underneath the related diagram.

REFERENCES

Aitken, D., and Roche, P. F. 1985, *M.N.R.A.S.*, **213**, 777.
Bezler, M., Kendziora, E., Staubert, R., Hasinger, G., Peitsch, W., Reppin, C., Trümper, J., and Vages, W. 1984, *Astr. Ap.*, **136**, 351.
Boisson, C. 1986, private communication.
Canfield, R. C., and Puetter, R. C. 1981, *Ap. J.*, **243**, 390.
Carleton, N. P., Willner, S. P., Rudy, R. J., and Tokunaga, A. T. 1984, *Ap. J.*, **284**, 523.
Cutrie, R. M., Wisniewski, W. Z., Rieke, G. H., and Lebofsky, M. J. 1985, *Ap. J.*, **296**, 423.
Davidson, K., and Netzer, H. 1979, *Rev. Mod. Phys.*, **51**, 715.
Edelson, R. A., and Malkan, M. A. 1986, *Ap. J.*, **308**, 59 (EM).
Elvis, M., Green, R. F., Bechtold, J., Schmidt, M., Neugebauer, G., Soifer, B. T., Matthews, K., and Fabbiano, G. 1986, *Ap. J.*, **310**, 291.
Fabbiano, G., Miller, L., Trinchieri, G., Longair, M. and Elvis, M. 1984, *Ap. J.*, **277**, 115.
Fabbiano, G., and Trinchieri, G. 1985, *Ap. J.*, **296**, 430.
Fabbiano, G., Willner, S. P., Carleton, N. P., and Elvis, M. 1986, *Ap. J. (Letters)*, **304**, L37.
Ferland, G. J. 1981, *Ap. J.*, **249**, 17.
Kendall, M., and Stuart, A. 1979, *The Advanced Theory of Statistics*, Vol. **2**, (4th ed,; London: Charles Griffin), chap. 27.
Kwan, J. 1986, *Ap. J.*, **305**, 679.
Kwan, J., and Krolik, J. H. 1981, *Ap. J.*, **250**, 478.
Lacy, J. H., *et al.* 1982, **256**, 75.
Landau, R., *et al.* 1986, *Ap. J.*, **308**, 78.
Lawrence, A., and Elvis, M. 1982, *Ap. J.*, **256**, 410.
Lebofsky, M. J., and Rieke, G. H. 1980, *Nature*, **284**, 410.
MacAlpine, G. M. 1985, in *Astrophysics of Active Galaxies and Quasi-stellar Objects*, ed. J. S. Miller (Mill Valley: University Science Books), p. 259.
Macklin, J. T. 1982, *M.N.R.A.S.*, **199**, 1119.
Madejski, G. M. 1985, Ph.D. thesis, Harvard University.
Malkan, M. A. 1984, in *X-ray and UV Emission from Active Galactic Nuclei*, ed. W. Brinkmann and S. Trümper (Garching bei München: Max-Planck-Institut für Extraterrestriche Physik), p. 121.
Malkan, M. A., and Sargent, W. L. W. 1982, *Ap. J.*, **254**, 22.
Moorwood, A. F. M. 1986, *Astr. Ap.*, **166**, 4.
Mushotzky, R. F. 1984, *Adv. Space Res.*, **3**, Nos. 10–12, p. 157.
Neugebauer, G., Oke, J., Becklin, E. E., and Matthews, K. 1979, *Ap. J.*, **230**, 79.
Petre, R., Mushotzky, R. F., Krolik, J. H., and Holt, S. S. 1984, *Ap. J.* **280**, 499.
Phillips, M. M. 1979, *Ap. J. (Letters)*, **227**, L121.
Phillips, M. M., Feldman, F. R., Marshall, F. E., and Wamsteker, W. 1979, *Astr. Ap.*, **76**, L14.
Piccinotti, G., Mushotzky, R. E., Boldt, E. A., Holt, S. S., Marshall, E. E., Serlemitsos, P. J., and Shafer, R. A. 1982, *Ap. J.*, **253**, 485.

Puetter, R. C., and Hubbard, E. N. 1985, *Ap. J.*, **295**, 394.
Rees, M. J., Begelman, M. C., and Blandford, R. D. 1981, in *Tenth Texas Symposium on Relativistic Astrophysics*, ed. R. Ramaty and F. C. Jones (New York: New York Academy of Sciences), p. 254.
Rees, M. J., Silk, J. I., Werner, M. W., and Wickramasinghe, N. C. 1969, *Nature*, **223**, 788.
Rieke, G. H. 1985, in *Astrophysics of Active Galaxies and Quasi-stellar Objects*, ed. J. S. Miller (Mill Valley: University Science Books), p. 235.
Rieke, G. H., and Lebofsky, M. J. 1979, *Ap. J.*, **227**, 710.
———. 1981, *Ap. J.*, **250**, 87.
Robson, E. I., Gear, W. K., Clegg, P. E., Ade, P. A. R., Smith, M. G., Griffin, M. J., Nolt, I. J., Radostitz, J. V., and Howard, R. J. 1983, *Nature*, **305**, 194.
Roche, P. F., Aitken, D. K., Phillips, M. M., and Whitmore, B. 1984, *M.N.R.A.S.*, **207**, 35.
Rowan-Robinson, M., and Crawford, J. 1986, *M.N.R.A.S.*, in press.
Rudy, R. J. 1984, *Ap. J.*, **284**, 33.
Rudy, R. J., LeVan, P. D., Puetter, R. C., Smith, H. E., and Willner, S. P. 1982, *Ap. J.*, **253**, 53.
Rudy, R. J., and Puetter, R. C. 1982, *Ap. J.*, **263**, 43.
Savage, B. D., and Mathis, J. S. 1979, *Ann. Rev. Astr. Ap.*, **17**, 73.
Shuder, J. M. 1981, *Ap. J.*, **244**, 12.
Stein, W. A., and Weedman, D. W. 1976, *Ap. J.*, **205**, 44.
Tananbaum, H., Wardle, J. F. C., Zamorani, G., and Avni, Y. 1983, *Ap. J.*, **268**, 60.
Véron-Cetty, M.-P., Véron, P., and Tarenghi, M. 1983, *Astr. Ap.*, **119**, 69.
Ward, M. J., Penston, M. V., Blades, J. C., and Turtle, A. J. 1980, *M.N.R.A.S.*, **193**, 563.
Ward, M., Elvis, M., Fabbiano, G., Carleton, N. P., Willner, S. P., and Lawrence, A. 1987, *Ap. J.*, submitted (Paper I).
Wilson, A. S., and Heckman, T. M. 1985, in *Astrophysics of Active Galaxies and Quasi-stellar Objects*, ed. J. S. Miller (Mill Valley: University Science Books), p. 39.
Wilson, A. S., Penston, M. V., Fosbury, R. A. E., and Boksenberg, A. 1976, *M.N.R.A.S.*, **177**, 673.
Worrall, D. M., Mushotzky, R. F., Boldt, E. A., Holt, S. S., and Serlemitsos, P. J. 1979, *Ap. J.*, **232**, 683.
Yee, H. K. C. 1980, *Ap. J.*, **241**, 894.
Zombeck, M. V. 1982, *Handbook of Space Astronomy and Astrophysics* (Cambridge: University Press), p. 136.

N. P. CARLETON, M. ELVIS, G. FABBIANO, and S. P. WILLNER: Harvard-Smithsonian Center for Astrophysics, 60 Garden St., Cambridge, MA 02138

A. LAWRENCE: School of Mathematical Sciences, Queen Mary College, University of London, Mile End Road, London E14NS, England

M. WARD: Department of Astronomy, University of Washington, Seattle, WA 98195